Japanese Journal of Applied Physics

REGULAR PAPER • OPEN ACCESS

Reconfigurable waveguide based on valley topological phononic crystals with local symmetry inversion via continuous translation

To cite this article: Md. Shuzon Ali *et al* 2023 *Jpn. J. Appl. Phys.* **62** SJ1002

OPEN ACCESS

Japanese Journal of Applied Physics **62**, SJ1002 (2023) **REGULAR PAPER**

https://doi.org/**10.35848/1347-4065/acae63**

Reconfigurable waveguide based on valley topological phononic crystals with local symmetry inversion via continuous translation

Md. Shuzon Ali, Motoki Kataoka, Masaaki Misawa, and Kenji Tsuruta*

Department of Electrical and Electronic Engineering, Okayama University, 3-1-1 Tsushima-naka, Kita-ku, Okayama 700-8530, Japan

*E-mail: tsuruta@okayama-u.ac.jp

Received November 16, 2022; revised December 21, 2022; accepted December 25, 2022; published online January 25, 2023

We proposed a reconfigurable valley topological acoustic waveguide constructed using a 2D phononic crystal (PnC) with C_{3v} symmetric arrangement of three rods in the unit cell. An interface between two types of PnCs with differently oriented unit cells exhibits high robustness of the valley transport of acoustic waves via the topologically protected state. Structural reconfiguration was introduced by the continuous translation of rod arrays in the PnCs. The topological phase transition in this translational change was quantitatively identified by the change in the Berry curvature. The translation of the rods leaves a dimer array at the interface, creating a localized/defective mode along the waveguide. Despite the presence of the localized mode, the acoustic wave can propagate along the reconfigurable waveguide the same as the original waveguide. The continuous translation of a rod array can be used to turn on and off the bandgap. This can be a new approach to design a robust acoustic device with a high reconfigurability. © 2023 The Author(s). Published on behalf of The Japan Society of Applied Physics by IOP Publishing Ltd

1. Introduction

Topologically protected wave mechanics in solids have become a new research topic regarding energy and/or information transfer via various carriers of quantum and classical matter, such as photons represented by optical waves[1,2] and phonons represented by acoustic or elastic waves.[3] Phononic crystals (PnC), which are structures that reveal topologically protected robustness, based on a unit cell with C_{3v} symmetry showing topological phase transitions in their dispersion[4] during the rotation of the unit cell structure. Essentially, the same phenomenon has been identified in quasi-two-dimensional PnC with a finite thickness, referred to as a phononic crystal plate.[5,6] Immunization against defects in topological phononic and photonic systems is of great interest because of their ability to confine or guide waves, which is desirable in various applications, such as wave filters,[7–9] waveguides,[10,11] and sensors.[12,13] The waveguide structure must be reconfigurable considering the active control of its functionality to use a topological waveguide in an integrated device. Some examples of such a reconfigurable structure for topological photonic waveguides can be found in recent literature. For example, the dynamic control of topological edge states in photonic crystals for robust energy transport has been demonstrated through the modification of the refractive index of a liquid crystal background medium.[14] Another type of topological photonic crystal has also been proposed based on a prototypical phase-change material $Ge_2Sb_2Te_5$ (GST225) at a particular frequency and reversibly switched between "on" and "off" by transiting the GST225 structural state.[15] The reconfigurability of structures for acoustic/elastic wave propagation has also been examined. Zhang et al. demonstrated topologically protected sound propagation in a reconfigurable manner by rotating three-legged unit cells without altering their lattice structure.[16] Additionally, another type of reconfigurability in a topological elastic wave insulator has been proposed and experimentally demonstrated.[17] These studies adopted the mechanical rotation of the unit cell orientation and filling/draining liquid into holes. Tian et al. presented a tunable valley PnC composed of hybrid channel-cavity cells with three tunable parameters.[18] Zhuang et al.[19] presented a methodology for the inverse design of reconfigurable topological insulators for flexural waves in plate-like structures. Feng et al.[20] and Laude et al.[21] proposed two-dimensional reconfigurable PnC that supports topologically protected edge states for Lamb waves. However, these reports required specific mechanisms for the reconfiguration of waveguide structures without losing their robustness. Considering the implementation of integrated devices, a simpler but versatile approach to control the structural changes in the reconfiguration is needed. Moreover, it is desirable to have quantitative indices to characterize and/or optimize the waveguide structure during the reconfiguration.

Recently, the Berry curvature have been found to be important in explaining the topological phase transition of the band in a unit cell. Additionally, the chirality of the acoustic field intensity arises from the Berry curvature of the Dirac band. A tunable phononic crystal plate with Y-shaped prisms is designed to support valley transport of elastic waves, in which elastic valley pseudo-spin states exhibit opposite chirality similar to electronic spin states, based on the analogy of the quantum valley Hall effect.[22] The presence of topological states is because of the non-trivial topological character of bulk electronic bands called the bulk-edge correspondence[23,24] and has been shown even in the case of a weak disorder. The quantization of the Hall conductance due to the edge states becomes stable because they are chiral. However, more versatile designs are necessary for quantum Hall (QH), quantum spin Hall (QSH), and quantum valley Hall effect to achieve non-trivial topological phononic bandgaps. For example, additional active components, such as rotating gyroscopes or the application of an external field, are needed to break the time-reversal symmetry in QH systems,[25–30] where the Berry curvature clearly reveals the chiral character of the edge mode. However, QSH systems require a double-Dirac cone achieved by the zone folding method[31–33] for high-symmetry points. They

also demonstrated the possibility of a topologically protected edge state. In 2018, Mei et al.[34] also investigated the non-trivial band topology phase transition for Lamb waves in a thin phononic crystal plate to realize the valley Hall effect in the low-frequency regime. In 2019, Kim et al.[35] proposed a GaAs-based valley PnC and demonstrated the control of the chiral characteristics of the bulk valley modes by rotating triangular holes in the unit cell through topological phase transition. In addition, they showed that topologically protected edge states at multiple frequency ranges can be characterized using the signs and distributions of the Berry curvature.

In this study, we propose a robust reconfigurable interface that can be constructed by shifting the rod array.[36,37] The band topology phase transition in this reconstruction is quantitatively identified through the Berry curvature. This study demonstrates a simple but practical scheme for designing a topological acoustic waveguide aiming at the development of highly integrated switchable acoustic devices. We perform numerical design and analyses based on the finite element method to construct and simulate our proposed reconfigurable topological acoustic waveguides. The robustness of the acoustic-wave propagation in the waveguide is shown to be preserved in the reconfigured interface, proving the versatility of the proposed scheme.

The organization of the paper is the following. In Chap. 2, we have first described our model that focuses on the translational shift of metallic rod from the initial position to reconfigured position. Secondly, we have highlighted the phononic band and the Berry curvature to characterize the modes in terms of the symmetry of the unit cell. Then, we have explained the phononic band properties of different types of interfaces. In Chap. 3, We have designed reconfigured waveguides and have examined their transmission properties through the comparisons with other waveguide structures. Finally, conclusions are given in Chap. 4.

2. Modeling and characterization

2.1. Translational shift of rod array for symmetry transformation

Initially, we constructed a uniform C_{3v} symmetric structure of an array of the unit cell with orientation $\alpha = 30°$. Then, we shifted one rod from all layers below the interface to construct $\alpha = -30°$ oriented rod array in the lower layer using continuous translation $\vec{T}$. As a result, the uniform phononic structure is shown to be reconfigured with an interface between the upward and downward convex with C_{3v} symmetric structure ($\alpha = 30°$ in the upper layer and $\alpha = -30°$ in the lower layer). The continuous translation of the rod leaves a dimer array in the path of the reconfigured interface, as shown in Figs. 1(a), and 1(b). The translation vector for shifting rod from the original position to another in a neighboring hexagonal unit cell of the reconfigurable structure can be expressed as $\vec{T} = \left(-\frac{1}{2}a, -\frac{\sqrt{3}}{2}a + 2\sqrt{3}r\right)$, where r is the radius of each circular rod.

2.2. Phononic band structure model and the Berry curvature

In our model, the unit cell structure is composed of three circular rods of solid material (stainless steel) arranged in a hexagonal lattice embedded in water, as shown in Fig. 2(a), which was proposed by Okuno et al.[38] by considering the ease of fabrication. We set the lattice constant $a = 2.2$ mm and the diameter of each circular rod $d = 0.7$ mm, which defines the radius of each circular rod as $r = d/2 = 0.35$ mm. The speed of sound and mass density are 1490 m s^{-1} and 1000 kg m^{-3} for water, and 5780 m s^{-1} and 7800 kg m^{-3} for stainless steel rods, respectively. The relative orientation (α) of the rod array in the hexagonal lattice characterizes the symmetry of the structure. At the angle $\alpha = 30°$, the unit cell structure illustrated in Fig. 2(b), the band structure shows valley-type dispersion at the K point, and the band gap opens around the frequency of 356–405 kHz, whereas the flipped band is observed for the unit cell structure with $\alpha = -30°$, as depicted in Fig. 2(e). Instead of a continuous change in α, the rotation of the rod array, a structural transformation between the structures, illustrated in Figs. 2(b) and 2(e) can also be undertaken by translational shifts, as proposed in the previous section and illustrated in Fig. 1

The symmetry breaking of the unit cell by the translation of a rod leads to the reduction in the symmetry, and it generates another band structure where the gap still opens, as shown in Figs. 2(c) and 2(d). Nevertheless, we show in the following section that the interface between the PnC with and without translation creates an edge mode. This implies that band gap closing alone cannot be the definitive measure to identify the bulk bands that lead to the emergence of an edge state after constructing interfaces. Instead, topologically invariant quantities are required for identification. We calculated the Berry curvature $\Omega(\vec{k})$ for the upper and lower bands than the gap near the K+ and K− points in the reciprocal space to determine the topological nature of bands for unit cell structures during the structural transformations. The prescription for numerical calculation is provided in the appendix. Figures 3(a)–3(d) show the Berry curvature distributions along the path in the Brillouin zone depicted in the inset of the figure for the unit cell structures during the translational shifting of a rod. These figures reveal that each sign of the Berry curvature around the K+ and K− points for the upper and lower bands are continuously flipped during the translational shift. The insets in the figure also show the pressure fields and the acoustic-intensity distributions at K+ and K− points indicating that the chiral state of each band was also continuously flipped by the translational shift.

2.3. Interface band properties of supercell

Figure 4(a) illustrates supercells with valley PnCs, in which each unit cell is composed of three circular rods in a C_{3v} symmetry structure with $\alpha = 30°$ and $\alpha = -30°$, as well as their band structure along k_x. The width and height of the supercells are defined as a, and $\frac{30a}{\sqrt{3}}$ respectively. The upper and lower layers, with differently oriented unit cells, were separated by a topological interface. Figure 4(a) shows an edge mode around 310–430 kHz where the two pseudo-spin modes appear at the K+ and K− points (near the K points in the Brillouin zone of a supercell), as expected from the Berry curvature analysis described in the previous section. For comparison, the supercell of a single crystal in C_{3v} symmetry with orientation $\alpha = 30°$, as shown in Fig. 4(b), is prepared, where the band gap appears around 356–405 kHz. Figure 4(c) depicts a supercell with partially shifted rods in the unit cell, where one rod was shifted in all the unit cells below the interface with translation vector $\vec{T}_{\text{partial}} = \left(-\frac{1}{4}a, -\frac{\sqrt{3}}{2}a + \frac{5\sqrt{3}}{2}r\right)$, where r is the radius of

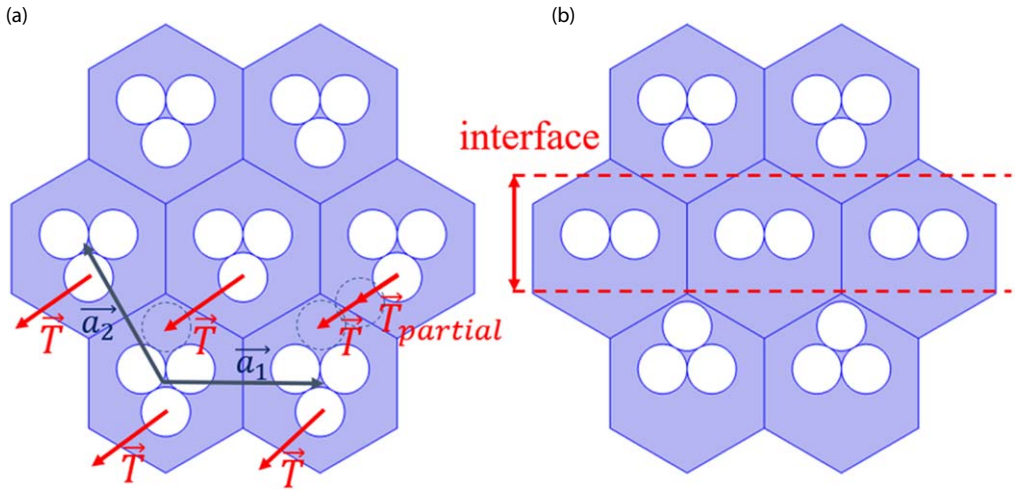

Fig. 1. (Color online) (a) Schematic of continuous translation of a rod array in a single phononic crystal, and (b) waveguide structure constructed after the transformation illustrated in (a).

each circular rod. A pressure field analysis on each band in Fig. 4(c) reveals that modes in the upper and lower band than the narrow band gap around 375–380 kHz are localized around the interface between two PnCs. Further continuous translation to $\delta\vec{T} = \left(-\frac{1}{4}a, -\frac{\sqrt{3}}{2}r\right)$ leads to a structural transformation from the original PnC with $\alpha = 30^\circ$ to the one with $\alpha = -30^\circ$ in the lower layer, as depicted in Fig. 4(d). We found that the band above 380 kHz near the K points is regarded as a bulk band, whereas the lower band than the frequency near the K points corresponds to a localized mode attributed to the presence of a dimer array at the interface. This can impact not only the wave transmission because of the localization of the mode, but also the band topology. Continuous translation breaks the local C_{3v} symmetry and creates a band gap, but the edge state may not necessarily appear around this frequency. Additionally, the continuous translation of the rods leaves a dimer array at the interface, creating a localized/defect mode and resulting in less energy transfer in the reconfigurable waveguide. In Fig. 4(e), we show another supercell structure with $\alpha = 30^\circ$ with one dimer array inserted into the structure to illuminate this localized mode effect. The nature of the flat band depicted at approximately 350 kHz near the K points in Fig. 4(e) corresponds to the mode localized around the interface.

Figure 4(f) shows that the band gap appears when a circular stainless steel rod is vertically shifted by 0.3 mm from each unit cell, and the local C_{3v} symmetry is reduced to C_{2v} symmetry. A pressure distribution analysis shows that the upper band at 380 kHz and lower band than the frequency near the K points are the localized band and bulk band, respectively. No edge state appears in the original gap frequency because the localized mode has a dominant effect in this frequency region. Based on these characterizations, we constructed valley phononic and reconfigurable phononic waveguides, which will be discussed in the following sections, to observe the robustness of wave propagations via the topologically protected edge state.

3. Design and transmission analysis of valley topological waveguides

One of the most important properties of topological wave devices is their robustness, as well as their ability to control the wave transmittance in the waveguide via the topological edge state. Based on the band structure design previously described, in this section, we examine the transmission properties of waveguides with various interface structures (Fig. 5) and the transmission spectra (Fig. 6).

3.1. Straight waveguide

First, we prepared a valley topological straight waveguide with 35 × 36 rectangular arrays of unit cells in C_{3v} symmetry with two different orientations, $\alpha = 30^\circ$ and $\alpha = -30^\circ$, respectively, and immersed them in water. Figure 5(a) shows the waveguide structure along with the pressure field distribution when an incident acoustic wave of 1 Pa at 400 kHz was input from the left port region and the transmittance was measured at the right (output). In Fig. 6(a), the red curve clearly shows that efficient wave transmission is realized around the bulk band-gap frequency range of 356–405 kHz, based on the band structure design in the previous section.

3.2. Reconfigurable waveguide

Next, we prepared 35 × 36 rectangular arrays of uniform phononic C_{3v} crystal structures with a single orientation $\alpha = 30^\circ$ to show that a topological waveguide can also be constructed by the continuous translation of the rod arrays proposed in the previous section. We observed the pressure field along this uniform waveguide, as illustrated in Fig. 5(b) at 400 kHz. No transmission is observed in this frequency range of 356–405 kHz, because no edge state appears, as depicted by the blue curve in Fig. 6(b). We partially shifted one rod from each unit cell in all layers using continuous translation $\vec{T}_{\text{partial}}$. Consequently, a symmetry-broken waveguide was constructed at the interface between the layers with and without partial translations. We measured the output pressure field of this partially shifted waveguide, as shown in Fig. 5(c), at 400 kHz. The yellow curve in Fig. 6(a) shows low transmission in the frequency range of 375–380 kHz. The PnC layer with $\alpha = -30^\circ$ oriented array is constructed by further continuous translation of the rod with $\delta\vec{T}$ below the interface. Thus, the uniform phononic structure is reconfigured to a waveguide with an interface between upward and downward convex with C_{3v} symmetric structure ($\alpha = 30^\circ$ in the upper layer and $\alpha = -30^\circ$ in the lower layer). The total translation vector for one shifted stainless steel rod from the

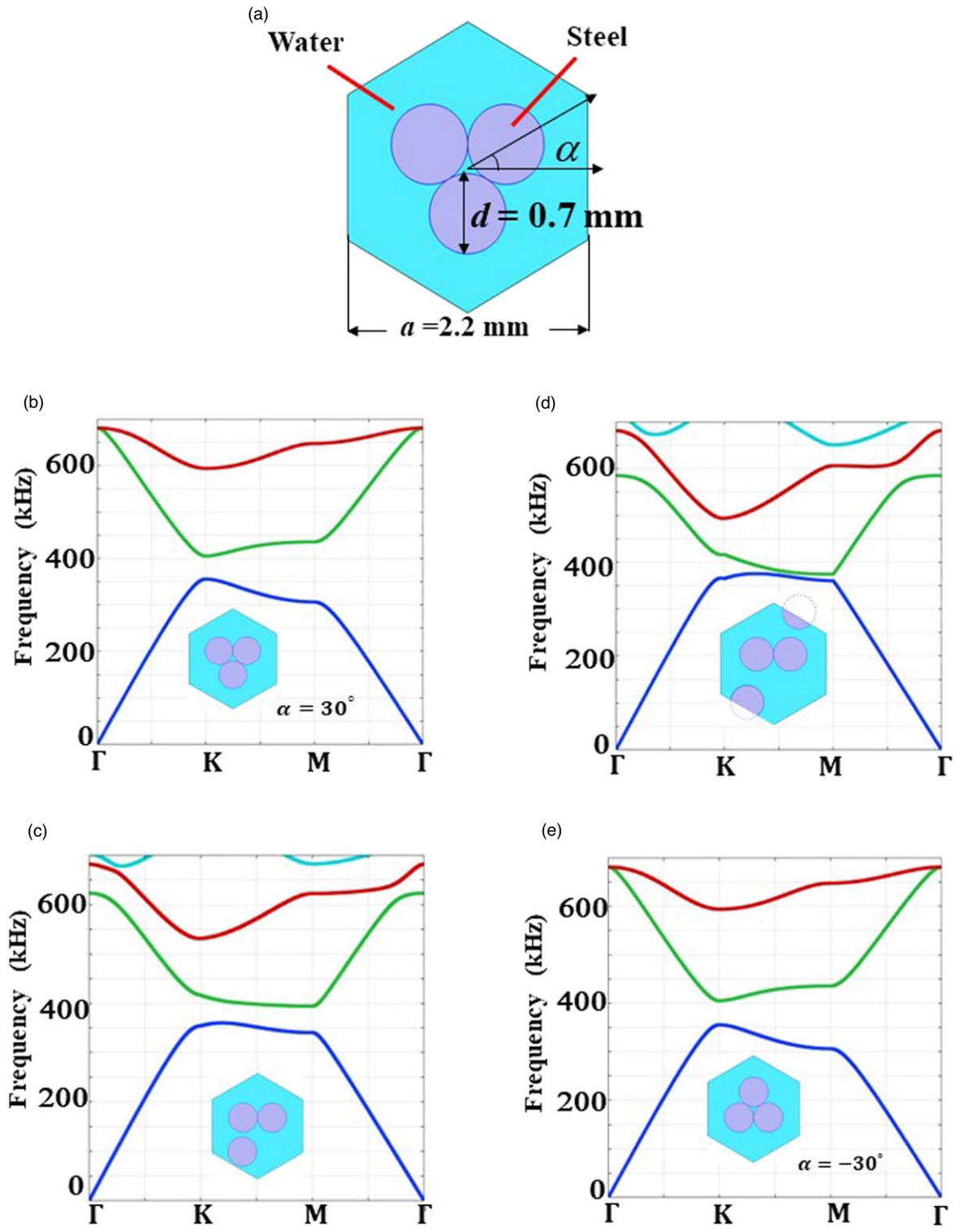

Fig. 2. (Color online) (a) Hexagonal unit cell with C_{3v} symmetry, and band structures (b) for the unit cell with α=30°, (c) for the unit cell with partially shifted rod, (d) for the unit cell with intermediate shift, and (e) for the unit cell with α=-30°.

initial position to the reconfigured position was $\overrightarrow{T}$ defined in Sect. 2.1. It should be noted that the continuous translation of rod leaves a dimer array with C_{2v} local symmetry in the waveguide, as illustrated in Fig. 1(b). Figure 5(d) depicts the reconfigured waveguide along with the pressure field distribution in the case where an incident acoustic wave at 400 kHz is input from the left port region, and the transmittance is measured at the output port at the right exit of the waveguide. We observed almost the same transmission of the reconfigured interface as that of the original valley topological waveguide, as depicted by the blue curve in Fig. 6(a). We constructed 35 × 36 rectangular arrays of stainless steel rod unit cells with C_{3v} symmetry structure with $\alpha = 30°$ orientation with a dimer array, as shown in Fig. 5(e), to determine the effect of the localized mode (defect) because of the dimer array left after the translational shift. No transmission was observed along this interface region of the C_{3v} crystal with the dimer array waveguide, as shown by the red curve in Fig. 6(b), revealing that the presence of the dimer array alone cannot generate a localized

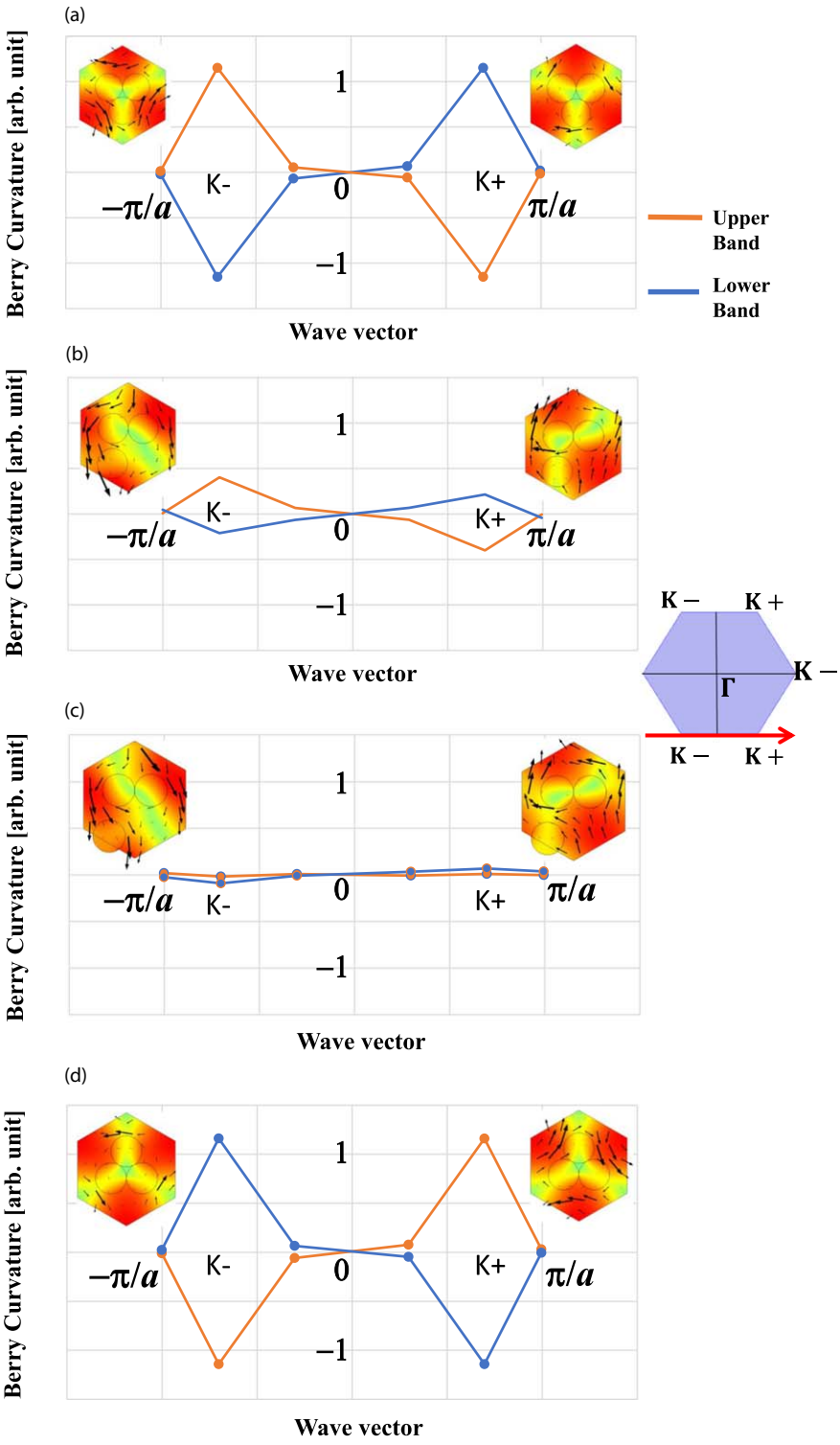

Fig. 3. (Color online) Berry curvatures of the lower and upper bands in the reciprocal space near the K+ and K− valleys (a) for the unit cell with $\alpha = 30°$, (b) for the unit cell with partially shifted rod array, (c) for the unit cell with intermediate shift, and (d) for the unit cell with $\alpha = -30°$. Insets show pressure fields (color) and acoustic-intensity distributions (arrow) of the mode at K+ and K− points.

mode that contributes to the transmission observed in the reconfigured waveguide in Fig. 5(d).

3.3. Transformation to C_{2v} symmetric interface

In this section, we examine the effect of another translation on transmission properties. The position of a stainless steel rod in the original C_{3v} unit cell was vertically shifted by $\delta y = -0.3$ mm from its original position. Subsequently, the original symmetry C_{3v} in the unit cell is reduced to C_{2v}. The above ($\alpha = 30°$) and below ($\alpha = -30°$) layers with C_{2v} symmetry were separated by a straight interface. Therefore, another type of phononic waveguide is constructed, as shown in Fig. 5(f). We observed the output pressure field and the transmittance with respect to the incident wave at 400 kHz. In Fig. 6(c), no transmission occurs in the frequency range

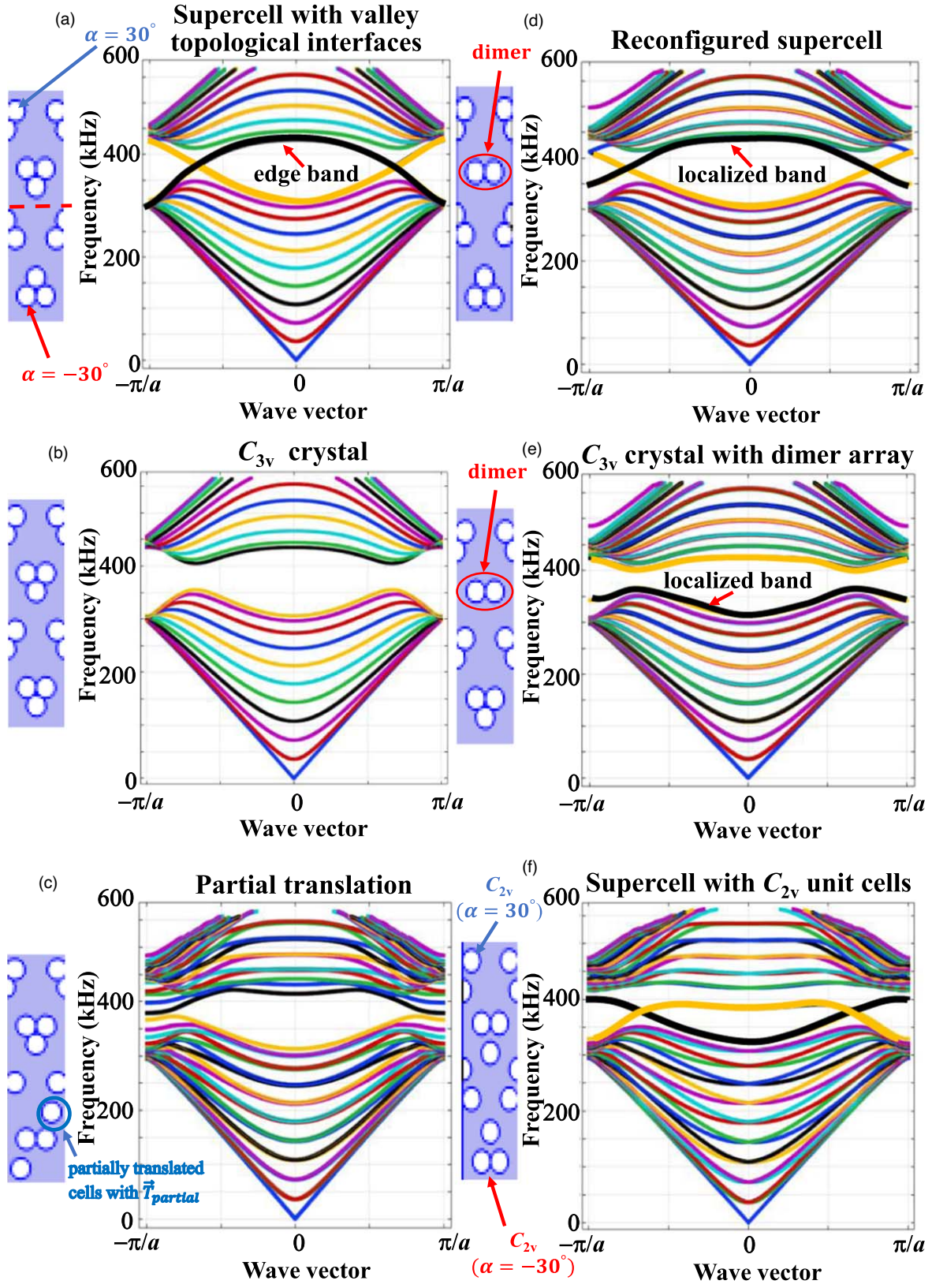

Fig. 4. (Color online) (a) Supercell structure and band diagrams of (a) a valley PnC with $\alpha = 30°$ and $\alpha = -30°$, (b) a PnC of uniform C_{3v} unit cells with $\alpha = 30°$, (c) supercell structure with partially shifted unit cells, (d) supercell with an interface between $\alpha = 30°$ and $\alpha = -30°$ reconfigured from the structure in (b) leaving a dimer array, (e) a PnC of uniform C_{3v} unit cells with $\alpha = 30°$ with dimer array inserted, and (f) supercell with an interface between two oppositely oriented ($\alpha = 30°$ and $-30°$) C_{2v} unit cells (generated by vertical shift with 0.3 mm).

390–430 kHz, indicating that no edge state is observed within the frequency range.

3.4. Z-shaped waveguides

We examined the transmission analysis for a Z-shaped waveguide that involves two corners, in which a large portion of transmission loss can be attributed to the propagation path, to demonstrate that the robustness can also be preserved by the present scheme of reconfiguration.[39] We arranged 27 × 18 rectangular array of unit cells with C_{3v} symmetry with two differently oriented rod arrays, $\alpha = 30°$ and

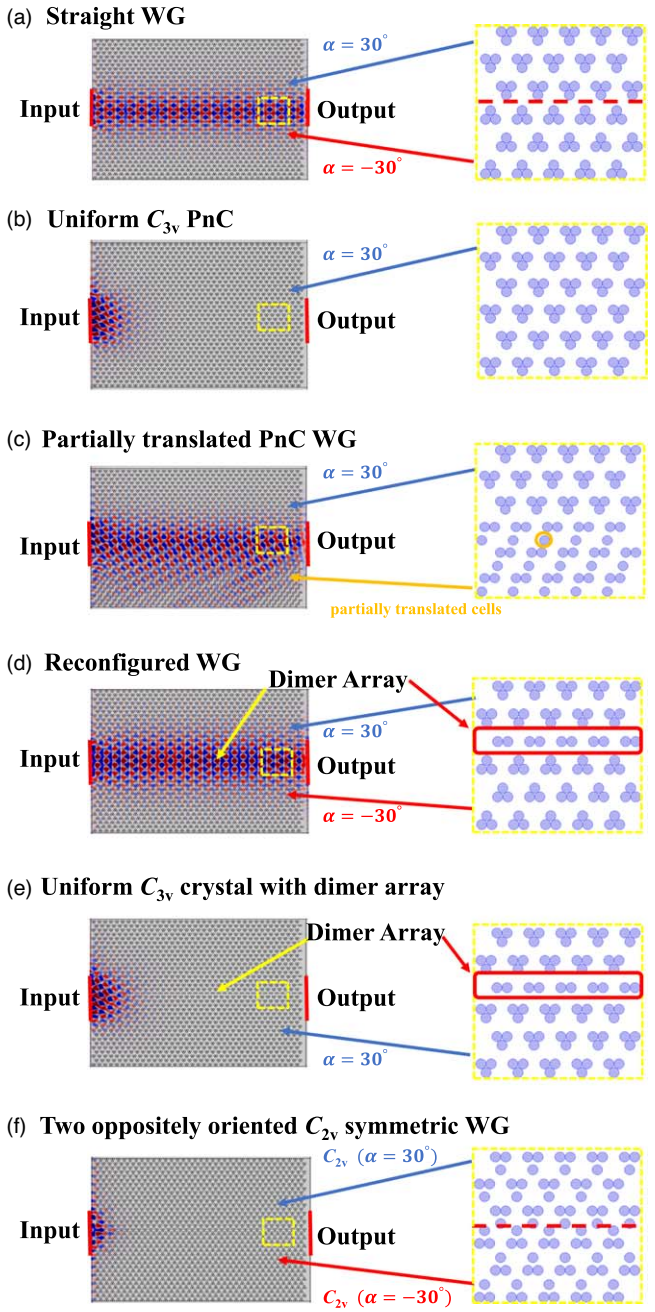

Fig. 5. (Color online) (Normalized) pressure fields for an incident wave at 400 kHz in (a) valley phononic straight waveguide (WG), (b) a uniform PnC, (c) WG with a partially shifted PnC, (d) a reconfigured WG, (e) a uniform PnC with a dimer array (to single out the localized mode effect on the pressure field), and (f) two oppositely oriented ($\alpha = 30°$ and $\alpha = -30°$) C_{2v} symmetric WG. The right side of each figure illustrates magnified views near the interface of each PnC structure (yellow dashed rectangle).

$\alpha = -30°$, respectively, in a two-dimensional hexagonal lattice and embedded in water. Then, we constructed a Z-shaped interface, as shown in Fig. 7(a), which is indicated by the yellow dotted lines. The lengths of both the upper and lower horizontal interfaces were $10 \times a = 22$ mm and $-10 \times a = -22$ mm, respectively, whereas the length of the oblique interface was $\frac{12 \times a}{\sqrt{3}} = 15.242$ mm. The waveguide structure and the pressure field distribution for an incident acoustic wave at 400 kHz are shown in Fig. 7(a). It exhibits efficient wave transmission (∼80%) within the frequency range of 356–405 kHz, as denoted by the blue curve in Fig. 7(c).

We also constructed a Z-shaped waveguide in a reconfigurable manner, as discussed in Sect. 2.2. Initially, we constructed a 27 × 18 rectangular array of unit cells with a uniform C_{3v} symmetric structure and $\alpha = 30°$ orientation and immersed them in water. We shifted one rod of each unit cell from the left half layer using a continuous translation $\vec{T} = \left(-\frac{1}{2}a, -\frac{\sqrt{3}}{2}a + 2\sqrt{3}\,r\right)$. Therefore, the C_{3v} symmetric unit cell with $\alpha = -30°$ is created and separated from $\alpha = 30°$ in the right-half layer by an oblique interface. We changed the current position of the top nine layers by translating $-\vec{T}$ to construct an $\alpha = 30°$ oriented unit cell. In addition, we changed the current position of the bottom nine layers with $\vec{T}$. Consequently, the uniform valley phononic structure with C_{3v} symmetry was reconfigured to a Z-shaped waveguide, as shown in Fig. 7(b). We observed the pressure field and the same wave transmittance along this interface region in the reconfigured Z-shaped waveguide. It is worth noting that the continuous translation of the rod leaves a dimer array, breaks the local symmetry, and slightly degrades the pressure field intensity in the Z-shaped path, as denoted by the orange curve in Fig. 7(c).

4. Conclusion

We proposed a design of the novel reconfigurable topological waveguide based on the translational shift of metallic steel rod arrays. Our results demonstrated that the band topology phase transition of the localized mode for symmetric breaking can be identified by observing the signs and distribution of the Berry curvature in the Brillouin zone. It is worth noting that the localized mode corresponding to the dimer array slightly degrades the pressure field in the path of the reconfigured waveguide interface. However, even when a localized mode is present in the reconfigured waveguide interface, the acoustic wave can still robustly propagate, which is comparable to an ideal valley phononic waveguide. Therefore, the valley support transport of acoustic energy can be controlled by designing a robust reconfigurable waveguide interface by shifting the rod array to the topologically protected edge state. An attempt for experimental verification is underway and will be reported elsewhere. The present approach can be used for a robust reconfigurable acoustic device based on a valley topological PnC.

Acknowledgments

This work was supported in part by JSPS KAKENHI (Grant Nos. JP21H05020 and JP21K18877).

Appendix

Berry curvature calculation

We highlighted the Berry curvature approach through the unit cell associated with both the upper and lower bands around the band gap to identify the topological phase for each

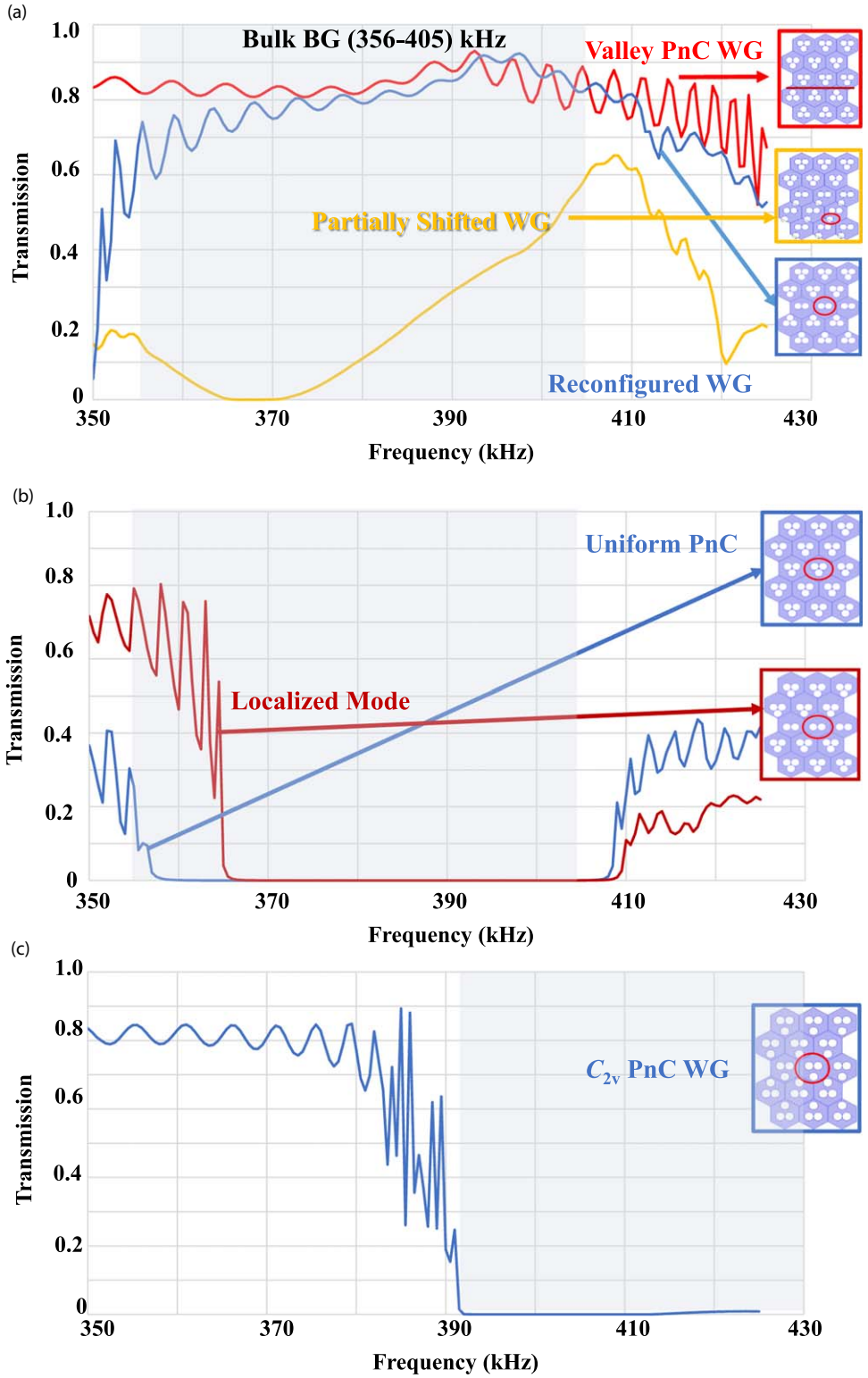

Fig. 6. (Color online) (a) Comparisons of the transmission in valley phononic waveguide (WG) (red), partially shifted WG (yellow), and reconfigured WG (blue). (b) Comparisons of the transmission in a uniform PnC (blue) and in a PnC with dimer array (red). (c) Transmission spectrum in symmetry-broken (C_{2v}) PnC WG.

phononic band. The Berry phase of the nth band along a closed path C is defined as

$$\gamma_n = \oint_C \vec{\Lambda}_n(\vec{k}).d\vec{k} = \iint_s \Omega_n(\vec{k})d^2k,$$

where $\vec{\Lambda}_n(\vec{k})$ is the Berry connection and $\vec{\Lambda}_n(\vec{k}) \equiv \langle u_n(\vec{k})|i\nabla_{\vec{k}}|\, u_n(\vec{k})\rangle$ and $\Omega_n(\vec{k}) = \nabla_{\vec{k}} \times \vec{\Lambda}_n(\vec{k})$ is the Berry curvature.[40] In our calculation, the Berry curvature at a certain point (k_x, k_y) in k space is expressed as[35,41]

$$\Omega(\vec{k}) = \frac{-\mathrm{Im}[\langle u(\vec{k}_1)|\, u(\vec{k}_2)\rangle + \langle u(\vec{k}_2)|\, u(\vec{k}_3)\rangle + \langle u(\vec{k}_3)|\, u(\vec{k}_4)\rangle + \langle u(\vec{k}_4)|\, u(\vec{k}_1)\rangle]}{\delta k_x \times \delta k_y},$$

where $\vec{k}_j (j = 1, 2, 3, 4)$ are four points of the rectangle surrounding a point in k space, creating a counterclockwise

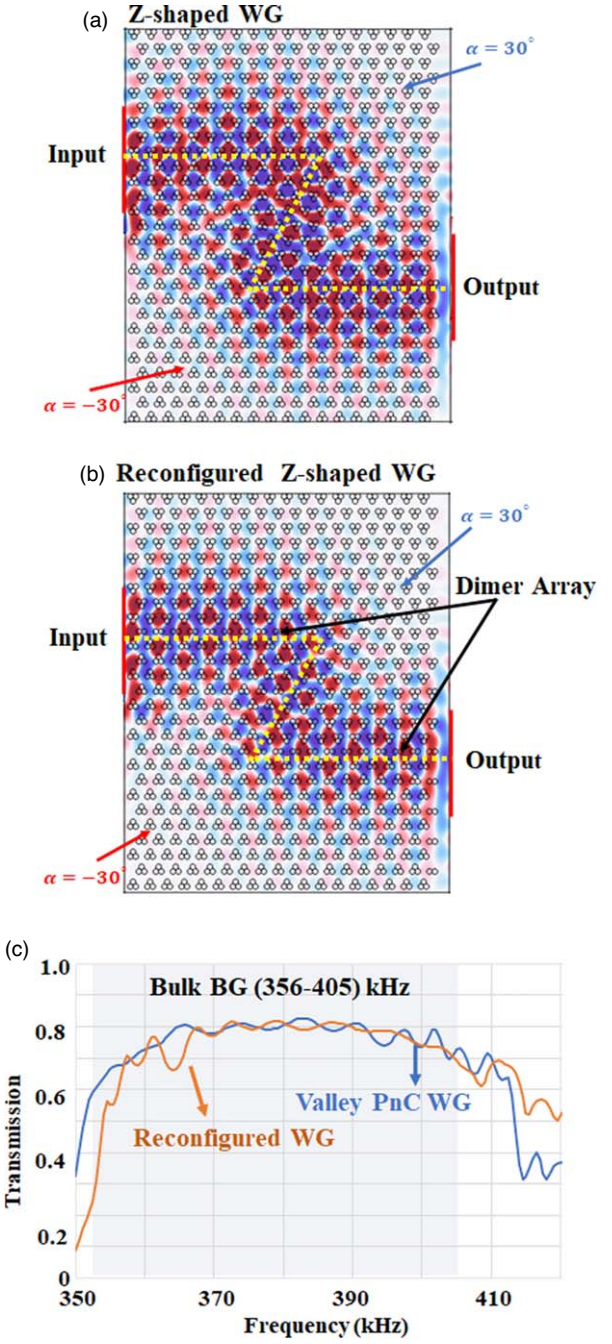

Fig. 7. (Color online) (Normalized) pressure fields (a) in a valley phononic Z-shape waveguide (WG) and (b) in reconfigured Z-shaped WG at 400 kHz. (c) Comparison of transmission spectrum in valley phononic (blue) and reconfigured (orange) Z-shaped WGs.

path: $\vec{k}_1\left(k_x - \frac{\delta k_x}{2}, k_y - \delta k_y/2\right)$, $\vec{k}_2\left(k_x - \frac{\delta k_x}{2}, k_y + \delta k_y/2\right)$, $\vec{k}_3\left(k_x + \frac{\delta k_x}{2}, k_y + \delta k_y/2\right)$, and $\vec{k}_4\left(k_x + \frac{\delta k_x}{2}, k_y - \delta k_y/2\right)$. The displacement vector field term $u_n(\vec{k})$ for the two-dimensional eigenmode. In our numerical calculation, all eigenmodes were normalized with respect to the integration of $\langle u_n(\vec{k})|\ u_n(\vec{k})\rangle$ over the surface of the unit cell.

ORCID iDs

Kenji Tsuruta https://orcid.org/0000-0002-1447-2530

1) Z. Wang, Y. Chong, J. D. Joannopoulos, and M. Soljacic, Nature **461**, 772 (2009).
2) Z. Wang and S. Fan, Appl. Phys. B **81**, 369 (2005).
3) R. Fleury, D. L. Sounas, C. F. Sieck, M. R. Haberman, and A. Alù, Science **343**, 516 (2014).
4) J.-C. Hsu and T.-T. Wu, Phys. Rev. B **74**, 144303 (2006).
5) A. Khelif, B. Aoubiza, S. Mohammadi, A. Adibi, and V. Laude, Phys. Rev. E **74**, 046610 (2006).
6) H. Zhu and F. Semperlotti, AIP Adv. **3**, 092121 (2013).
7) B. Rostami-Dogolsara, M. K. Moravvej-Farshi, and F. Nazari, Phys. Rev. B **93**, 014304 (2016).
8) H.-W. Dong, Y.-S. Wang, and C. Zhang, Ultrasonics **76**, 109 (2017).
9) T.-C. Wu, T.-T. Wu, and J.-C. Hsu, Phys. Rev. B **79**, 104306 (2009).
10) Y. Jin, N. Fernez, Y. Pennec, B. Bonello, R. P. Moiseyenko, S. Hémon, Y. Pan, and B. Djafari-Rouhani, Phys. Rev. B **93**, 054109 (2016).
11) R. Lucklum, M. Ke, and M. Zubtsov, Sensors Actuators B **171**, 271 (2012).
12) T.-X. Ma, Y.-S. Wang, C. Zhang, and X.-X. Su, Sensors Actuators A **242**, 123 (2016).
13) D. Jia, H.-X. Sun, J.-P. Xia, S.-Q. Yuan, X.-J. Liu, and C. Zhang, New J. Phys. **20**, 09302 (2018).
14) M. I. Shalaev, S. Desnavi, W. Walasik, and N. M. Litchinitser, New J. Phys. **20**, 023040 (2018).
15) T. Cao, L. Fang, Y. Cao, N. Li, Z. Fan, and Z. Tao, Sci. Bull. **64**, 814 (2019).
16) Z. Zhang, Y. Tian, Y. Chen, Q. Wei, X. Liu, and J. Christensen, Phys. Rev. Appl. **9**, 034032 (2018).
17) A. Darabi and M. Leamy, J. Acoust. Soc. Am. **146**, 773 (2019).
18) Z. Tian, C. Shen, J. Le, E. Reit, H. Bachman, J. E. S. Socolar, S. A. Cummer, and T. J. Huang, Nat. Commun. **11**, 762 (2020).
19) X. Zhuang, C. Nguyen, S. S. Nanthakumar, L. Chamoin, Y. Jin, and T. Rabczuk, Mater. Design **219**, 110760 (2022).
20) L.-Y. Feng, H.-B. Huang, J.-C. Zhang, X.-P. Xie, and J.-J. Chen, Phys. Lett. A **382**, 2880 (2018).
21) Y.-F. Wang, L. Yang, T. Wang, A.-L. Chen, and V. Laude, Appl. Materials **9**, 081110 (2021).
22) N. Gao, S. Qu, L. Si, J. Wang, and W. Chen, Appl. Phys. Lett. **118**, 063502 (2021).
23) Y. Hatsugai, Phys. Rev. Lett. **71**, 3697 (1993).
24) Y. Hatsugai, T. Fukui, and H. Aoki, Phys. Rev. B **74**, 205414 (2006).
25) A. B. Khanikaev, R. Fleury, S. H. Mousavi, and A. Alù, Nat. Commun. **6**, 8260 (2015).
26) Z. Yang, F. Gao, X. Shi, X. Lin, Z. Gao, Y. Chong, and B. Zhang, Phys. Rev. Lett. **114**, 114301 (2015).
27) Z. G. Chen and Y. Wu, Phys. Rev. Appl. **5**, 054021 (2016).
28) X. Ni, C. He, X. C. Sun, X. P. Liu, M. H. Lu, L. Feng, and Y. F. Chen, New J. Phys. **17**, 053016 (2015).
29) L. M. Nash, D. Kleckner, A. Read, V. Vitelli, A. M. Turner, and W. T. M. Irvine, Proc. Natl Acad. Sci. **112**, 14495 (2015).
30) P. Wang, L. Lu, and K. Bertoldi, Phys. Rev. Lett. **115**, 104302 (2015).
31) R. Chaunsali, C. W. Chen, and J. Yang, Phys. Rev. B **97**, 054307 (2018).
32) S. Y. Yu, C. He, Z. Wang, F. K. Liu, X. C. Sun, Z. Li, H. Z. Lu, M. H. Lu, X. P. Liu, and Y. F. Chen, Nat. Commun. **9**, 3072 (2018).
33) C. Brendel, V. Peano, and F. Marquardt, Phys. Rev. B **97**, 020102(R) (2018).
34) J. Wang and J. Mei, Appl. Phys. Express **11**, 057302 (2018).
35) I. Kim, Y. Arakawa, and S. Iwamoto, Appl. Phys. Express **12**, 047001 (2019).
36) K. Okuno, M. Misawa, and K. Tsuruta, Proc. Symp. on Ultrason. Electron. **41**, 3Pa1-2 (2020).
37) M. S. Ali, M. Kataoka, M. Misawa, and K. Tsuruta, Proc. Symp. on Ultrason. Electron. **43**, 1Pa1-3 (2022).
38) K. Okuno and K. Tsuruta, Jpn. J. Appl. Phys. **59**, SKKA05 (2020).
39) M. Kataoka, M. Misawa, and K. Tsuruta, Symmetry **14**, 2133 (2022).
40) D. Xiao, M.-C. Chang, and Q. Niu, Rev. Mod. Phys. **82**, 1959 (2010).
41) T. Fukui, Y. Hatsugai, and H. Suzuki, J. Phys. Soc. Jpn. **74**, 1674 (2005).